The Role of Iron in the Formation of Porosity in Al-Si-Cu–Based Casting Alloys: Part II. A Phase-Diagram Approach

J.A. TAYLOR, G.B. SCHAFFER, and D.H. StJOHN

The mechanism by which iron causes casting defects in the AA309 (Al-5 pct Si-1.2 pct Cu-0.5 pct Mg) may be related to the solidification sequence of the alloy. Superimposing calculated segregation lines on the liquidus projection of the ternary Al-Si-Fe phase diagram suggests that porosity is minimized at a critical iron content when solidification proceeds directly from the primary field to the ternary Al-Si-βAl$_5$FeSi eutectic point. Solidification *via* the binary Al-βAl$_5$FeSi eutectic is detrimental to casting integrity. This hypothesis was tested by comparing the critical iron content observed in the standard AA309 alloy to that of a high-silicon (10 pct Si) variant of this alloy.

I. INTRODUCTION

IRON is known to cause porosity and shrinkage defects in Al-Si–based casting alloys. It has been suggested[1–4] that the intermetallic phase β-Al$_5$FeSi is the primary cause of this porosity. The "restricted feeding theory"[1,2,3] suggests that β platelets interfere with liquid feeding, whereas the "pore nucleation theory"[4] suggests that the β platelets are active sites for pore nucleation. Both of these theories imply that porosity should increase monotonically with iron content. However, the results from Part I of this study[5] clearly indicate that this is not the case. While we found that porosity formation is a function of the iron concentration, a complex threefold effect was also identified. For an unmodified, non-grain-refined, Al-5.2 pct Si-1.2 pct Cu-0.5 pct Mg alloy (Australian designation AA309; all compositions given in wt pct), the specific features of this effect are that

(1) the total porosity is minimized at 0.4 pct Fe,
(2) a localized shrinkage-porosity defect (termed the "extended defect") develops at iron concentrations greater than 0.4 pct under nonoptimum casting conditions, and
(3) there is a change from a discrete pore morphology at 0.1 pct Fe content to zones of spongelike interdendritic porosity at higher iron levels.

The previous theories are clearly inadequate in explaining these observations. In this article, we propose an alternative model based on the Al-Fe-Si phase diagram and the corresponding solidification sequences. We also test the predictions of this model using an Al-10 pct Si alloy. The microstructural basis for this hypothesis is discussed elsewhere.[6]

II. A SOLIDIFICATION MODEL

Equilibrium solidification is based on the assumption that diffusion in both the liquid and solid phases is infinitely fast and that equilibrium concentrations are maintained in both phases at all times.[7] It requires the following condition to be maintained for each element:

$$C_L = \frac{C_O}{1 + f_S(k - 1)} \qquad [1]$$

where C_O and C_L are the concentrations of each element in the original melt and in the decreasing liquid phase, respectively; f_S is the instantaneous fraction solid; and k is the partitioning coefficient for the element.

Solidification based on the nonequilibrium lever rule follows the Scheil equation[7] and is founded on the assumption that there is complete diffusion within the liquid phase but that no diffusion occurs in the solid phase. The concentration of each element in the liquid is then

$$C_L = C_O(1 - f_S)^{(k-1)} \qquad [2]$$

A third solidification model assumes full diffusion within the liquid but only partial diffusion within the solid. The modified equations of Clyne and Kurz[8] give the concentrations as

$$C_L = C_O\{1 - (1 - 2\alpha' k)f_S\}^{(k-1)(1-2\alpha' k)} \qquad [3]$$

where α' is the back-diffusion parameter, defined by

$$\alpha' = \alpha(1 - e^{-1/\alpha}) - 0.5e^{-1/2\alpha} \qquad [4]$$

where $\alpha = D_s t_f/L^2$, D_s is the solid-state diffusion coefficient of the element, t_f is the local solidification time, and L is the size of the solidifying system. For equiaxed microstructures, L = SDAS/2, where SDAS is the secondary dendrite arm spacing. The values of these parameters for the experimental conditions used here are

$k_{Fe} = 0.02$ and $k_{Si} = 0.11$,

$D_{Fe} = 5.3 \times 10^{-3} \exp(-183.4 \text{ kJ mol}^{-1}/\text{R}T)$ (measured in m^2/sc),

$D_{Si} = 2.0 \times 10^{-4} \exp(-133.5 \text{ kJ mol}^{-1}/\text{R}T)$ (measured in m^2/sc),

R = 8.31×10^{-3} (the universal gas constant, measured in kJ mol^{-1} K^{-1}),

T = 873 K (a constant value chosen to best represent a variable),

t_f = 360 seconds (approximate solidification time of the extended-defect region in the experimental castings described elsewhere[5]), and

J.A. TAYLOR, formerly Doctoral Student, is Senior Research Fellow, CRC for Alloy and Solidification Technology (CAST), Department of Mining, Minerals and Materials Engineering, The University of Queensland. G.B. SCHAFFER, Reader, and D.H. StJOHN, Professor, are with CAST, Department of Mining, Minerals and Materials Engineering, The University of Queensland, Brisbane, QLD 4072, Australia.

Manuscript submitted March 27, 1998.

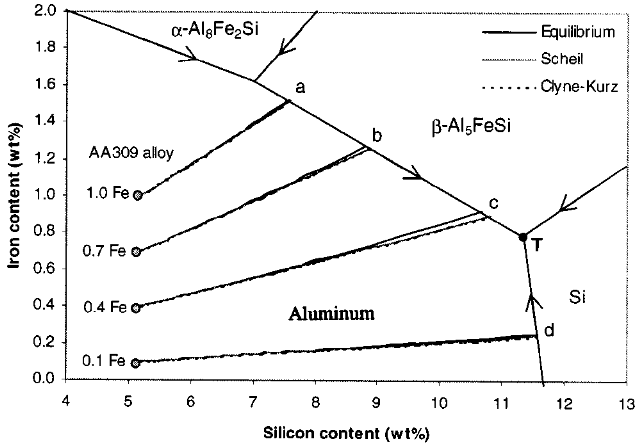

Fig. 1—The segregation lines (*i.e.*, freezing/solidification paths) across the liquidus surface of the Al-Fe-Si ternary phase diagram, calculated according to three solidification models for AA309 alloy with various iron contents. The values of fraction solid at the intersections with the eutectic troughs at points a, b, c, and d are approximately 35, 46, 57, and 61 pct, respectively. The precise position of the ternary eutectic point, *T*, is disputed.

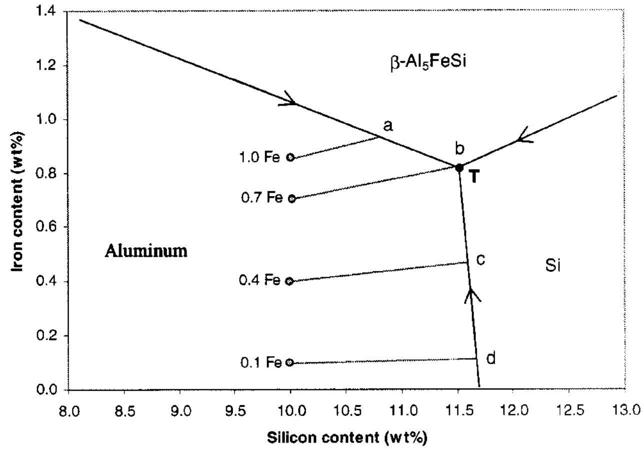

Fig. 2—The segregation lines (solidification paths) across the liquidus surface of the equilibrium Al-Fe-Si ternary phase diagram for a 10 pct silicon alloy with various iron contents, calculated according to the Scheil equation. The fraction solid values at the intersections with the binary eutectic troughs, designated points a, b, c, and d are approximately 8, 14, 15, and 16 pct, respectively.

SDAS $= 80$ μm (value obtained at B7 for the one riser without chill (1RNC) casting, AA309, 0.40 pct Fe)

Using these values in Eq. [1] through [3] allows the calculation of segregation lines. These are superimposed over the liquidus projection of an abridged Al-Fe-Si ternary equilibrium-phase diagram in Figure 1. It is evident from this figure that there is very little difference between the different solidification paths obtained by the three methods. This validates the method of Backerud *et al.*,[9] who used the ternary Al-Fe-Si phase diagram and a set of segregation lines derived from the Scheil equation to represent the solidification paths for all iron-containing hypoeutectic Al-Si–based 300-series alloys, regardless of the copper or magnesium content. Their approach is, therefore, followed here.

The critical defect-prone region in the castings prepared during the previous experimental work[5] experienced relatively slow cooling rates, *e.g.*, 0.3 °C/s to 0.4 °C/s. The use of the equilibrium-phase diagram is, therefore, a reasonable approximation. Nevertheless, a few limiting factors remain.

(1) The precise composition of the ternary eutectic point of the Al-Fe-Si system is disputed, with ranges from 0.4 to 1.0 pct Fe and 11.3 to 12.0 pct Si.[10] The value of 11.5 pct Si and 0.80 pct Fe, as proposed by Phillips and Varley[11] and favored by others,[9,10] is used in this article.
(2) The position of the binary Al-Si eutectic line is affected by both the cooling rate and the presence of small amounts of chemical-modifying elements and is, therefore, poorly defined.
(3) The position of the triple point between the aluminum, α-Al_8Fe_2Si, and β-Al_5FeSi phase fields is sensitive to the cooling rate and to the presence of impurities such as Mn.
(4) Elements such as Cu and Mg, present in the AA309 alloy, are known to alter the ternary eutectic temperature.[12] Whether they also displace the composition of any of these critical points is unclear, although Backerud *et al.*[9] ignore any effect.

Figure 1 suggests by interpolation that, at approximately 0.35 pct Fe in AA309, solidification proceeds from the primary aluminum phase field directly to the ternary Al-Si-βAl_5FeSi point. At lower iron concentrations, solidification occurs *via* the Al-Si binary eutectic valley, whereas, at higher iron concentrations, solidification occurs *via* the Al-βAl_5FeSi binary eutectic valley. The possible solidification sequences are

Fe $<$ 0.35 pct: Liquid $\rightarrow$ Al $\rightarrow$ Al-Si binary $\rightarrow$ Al-Si-Al_5FeSi ternary,

Fe $=$ 0.35 pct: Liquid $\rightarrow$ Al $\rightarrow$ Al-Si-Al_5FeSi ternary, and

Fe $>$ 0.35 pct: Liquid $\rightarrow$ Al $\rightarrow$ Al-$A1_5FeSi$ binary $\rightarrow$ Al-Si-Al_5FeSi ternary.

The iron concentration at which the solidification sequence changes is, therefore, defined as the critical point (Fe_{crit}).

The previous experimental work[5] indicated that the lowest level of porosity formed at 0.4 pct Fe. The proximity of this empirical value to Fe_{crit} suggests that porosity may be minimized when solidification proceeds from primary dendrite formation directly to the ternary eutectic. Any deviation from this solidification path encourages porosity formation. Although deviations arising from lower iron contents result in increased total porosity, it is the deviations at higher iron contents that are of greatest concern. The severity of the resultant shrinkage defects is dependent on the distance of the intersection point (*i.e.*, where the solidification path intersects a eutectic valley and changes direction) from the ternary eutectic point. The further the intersection point from the ternary eutectic, the more pronounced are the defect-forming effects.

Given that the segregation lines are alloy dependent, it should be possible to use this model to predict porosity-prone solidification paths in Al-Si–based alloys. Furthermore, it should also be possible to predict the actual critical iron level for different base alloy compositions. This would allow the model to be experimentally tested. To this end, segregation lines are superimposed in Figure 2 on the liquidus projection of the Al-Fe-Si phase diagram for an Al-10 pct Si alloy. Because there is no significant difference between

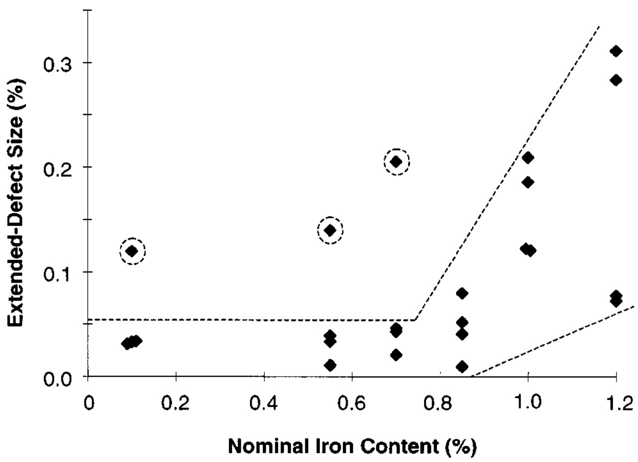

Fig. 3—Extended-defect size *vs* nominal iron content for 1RNC castings produced with the 10 pct silicon-containing alloy. The scatterbands (dotted lines) are not statistically derived and have been drawn assuming that the three circled points are abnormal in some respect. See text for details.

the three segregation models in this system, only the Scheil lines are plotted in this figure. From this construction, the critical iron level for an Al-10 pct Si alloy should be 0.7 pct. The implication is that a porosity minimum should occur at 0.7 pct Fe and that extended-defect formation should only become apparent at richer iron levels.

III. EXPERIMENTAL

Alloy preparation, casting procedures, and analytical testing methods have been described in detail in Part I of this article.[5] However, conditions specific to this article are described subsequently.

The 10 pct silicon-containing alloy was prepared from the base AA309 ingot with an addition of low-impurity metallurgical-grade silicon metal, such that the final alloy composition was approximately Al-10 pct Si-1.15 pct Cu-0.5 pct Mg-0.1 pct Fe. The crushed silicon and the ingot charge were melted together in a clay-bonded graphite crucible in a 20 kV induction furnace. Complete dissolution was accomplished by holding the melt for 10 minutes at 740 °C (the same period in which any iron additions were also made). After following the standard thermal regime, the alloy was cast at 715 °C (the pouring temperature that allowed a melt of near-liquidus temperature, i.e. 580 °C, to reach the "chill" end of the casting before inversion of the mold).

A total of 28 cylindrical castings were produced in the 1RNC configuration (using a variant of the improved low-pressure casting technique described in Part I of this article[5]) at iron contents of 0.1, 0.4, 0.55, 0.7, 0.85, 1.0, and 1.2 pct. In addition, a further six castings were made in the two riser without chill (2RNC) configuration at iron contents of 0.1 pct (four castings) and 1.0 pct (two castings).

Porosity profile determination, optical metallography (both qualitative and quantitative), and cooling-curve analysis were carried out in a similar manner to that described previously.[5]

IV. RESULTS

Porosity profiles were determined for each of the castings, and the average values of total porosity, background porosity,

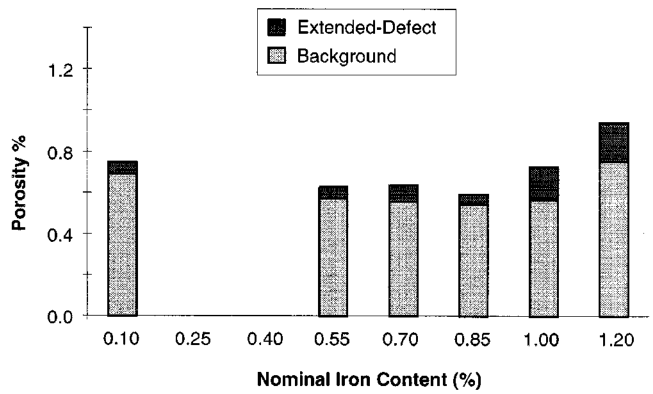

Fig. 4—The average contributions of both the extended-defect and the background porosity to the total casting porosity *vs* the nominal iron content for the 1RNC 10 pct Si alloy castings (including the three possible outlying points shown in Fig. 3).

and extended-defect size were calculated for each of the experimental iron contents. The definition of the extended defect is described elsewhere.[5] It is essentially the size of the localized defect peak (over several adjacent casting segments) above a hypothetical smooth background-porosity profile that would have been evident in its absence.

The effect of iron is manifest in the size of this extended defect. It is plotted in Figure 3 as a function of the iron content for the poorest casting condition tested (1RNC). All the data collected, including three possible outlying points, are indicated in this figure. The sum of the average extended-defect size and the average background porosity is plotted as a function of iron content in Figure 4 (for all data points) and in Figure 5 (outlying data points omitted). It is apparent from these figures that the least porosity occurs at either 0.85 pct Fe (Figure 4) or 0.7 pct Fe (Figure 5) and that, when the outlying points are ignored, the extended defect only occurs at iron contents greater than 0.7 pct. These trends and values are as predicted. The justification for the omission of the outlying points is discussed later.

The extended defect in the high-silicon alloy was not as precisely located in the B7 region as it was in the lower silicon AA309 alloy. Rather, the extended defect was more often spread over a wider area, with a slightly offset focus around segment C6. This is illustrated in Figure 6.

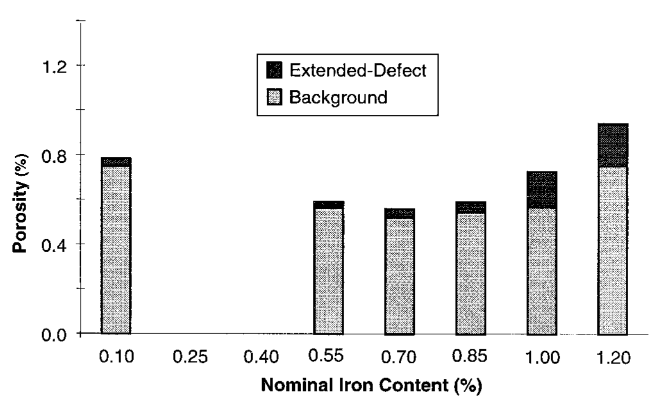

Fig. 5—The average corrected contributions of both the extended-defect and the background porosity to the total casting porosity *vs* the nominal iron content for the 1RNC 10 pct Si alloy castings. The corrections are obtained by neglecting the three outlying points shown in Fig. 3.

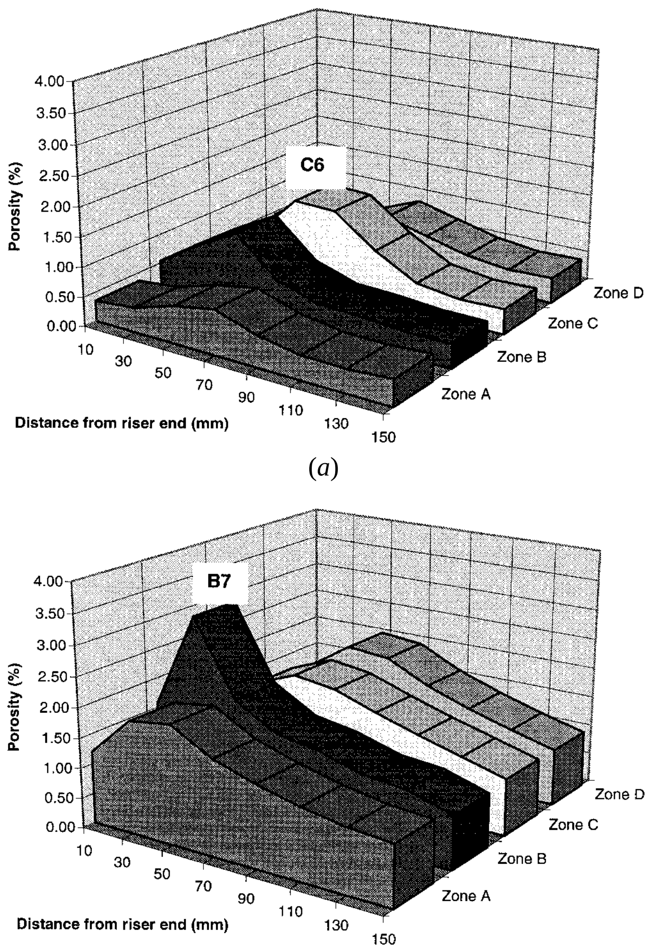

Fig. 6—Porosity profiles of two individual casts: (*a*) 10 pct Si alloy with 1.20 pct Fe and (*b*) AA309 alloy with 1.00 pct Fe. The example in (a) shows a broad defect shifted toward segment C6, while (b) shows a tighter defect located around B7.

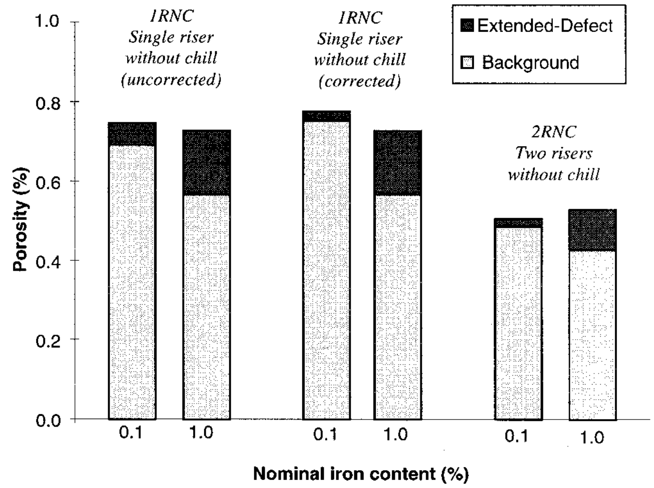

Fig. 7—The average contributions of background porosity and extended-defect size to the total casting porosity in 10 pct silicon alloy castings at two different iron contents in two different casting configurations.

The background porosity and the size of the extended defect for the 2RNC configuration was also evaluated for 0.1 and 1.0 pct Fe levels in the Al-10 pct Si alloy. These results are presented in Figure 7. Adding a second riser decreases the total porosity observed, although it does not prevent the formation of the extended defect at the highest iron level. In the 2RNC castings with 0.1 pct Fe, there was no evidence of extended-defect formation. By contrast, an observable extended defect did form at even this lowest iron level in the 1RNC configuration.

Optical metallography revealed that the porosity in the defect-prone segments was predominantly of the spongy interdendritic type. The discrete, individual pores of rounded-to-elongated shape, observed previously in alloy AA309 with 0.1 pct Fe content,[5] were not so obviously present in the 10 pct silicon alloy with 0.1 pct Fe, although there was indication of a mixture of discrete and interconnected pore types. The wide range of porosity levels observed at the subcritical iron contents (*i.e.*, including outlying points) makes categorization of iron-related morphological changes difficult (*cf* the AA309 alloy). However, it is evident that extensive interconnection of sponge porosity regions does occur at the super critical iron contents of 1.0 and 1.2 pct.

Quantitative metallography of the iron-containing β and π intermetallic particle sizes and numerical density revealed an approximately linear increase in both of these parameters with increasing iron content.

Cooling-curve analysis of a solidifying casting (Al-10 pct Si containing 0.85 pct Fe) indicated that directional solidification occurs from the chill end toward the riser in the 1RNC configuration. The range of local cooling rates measured was from 0.40 °C/s to 0.21 °C/s at B1 and B8, respectively. However, because of the greatly extended period of eutectic solidification in the 10 pct silicon alloy (240 seconds at B7 (*cf* that of 110 seconds at B7 for AA309)), the thermal gradients effectively drop to zero in many regions of the casting for prolonged periods.

V. DISCUSSION

The observation that increasing the silicon content from 5 to 10 pct changes the onset of the iron-related shrinkage defect from 0.4 to 0.7 pct serves to validate the hypothesis that the solidification sequence controls the formation of porosity. Porosity is minimized if solidification proceeds directly from primary dendrite formation to the ternary Al-Si-βAl_5FeSi eutectic point. Furthermore, a highly localized defect can occur when solidification proceeds *via* the binary Al-βAl_5FeSi eutectic. As presented in Figures 3 through 5, however, this trend is most apparent in the Al-10 pct Si alloy when certain outlying points are omitted from the analysis. This approach is valid, because there is strong evidence that the outlying points arise as a consequence of the porosity formation becoming dominated by poor casting conditions rather than by alloy chemistry.

Porosity results from the 10 pct silicon alloy castings made using the improved feeding conditions (2RNC) show a more distinct influence of iron additions than was observed in the 1RNC condition. In the 2RNC case, the 0.1 pct Fe alloy showed a reduced tendency toward significant extended-defect formation (Figure 7). This suggests that the outlying extended-defect formation in the Al-10 pct Si alloy at subcritical iron contents, in the 1RNC configuration, is the result of insufficient feeding capacity for this particular alloy (*cf*

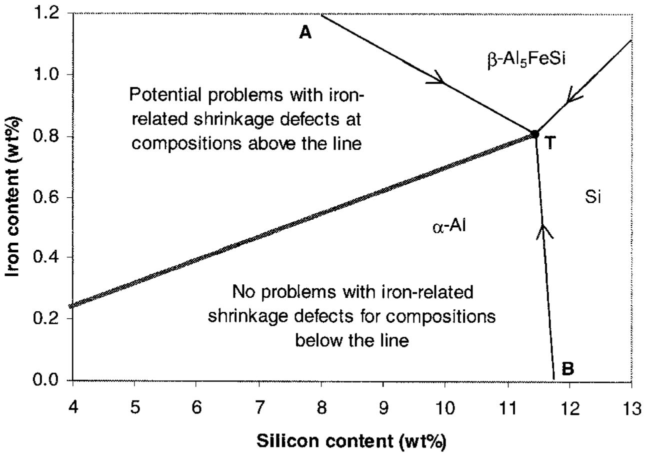

Fig. 8—A portion of the liquidus projection of the Al-Fe-Si ternary phase diagram showing the calculated line (bold) that defines the compositions at which the solidification sequence, according to the Scheil equation, proceeds directly from aluminum dendrite formation to the ternary eutectic formation (at point T) without traveling along one of the binary eutectic troughs (either AT or BT). To ensure that serious iron-related shrinkage porosity defects do not occur, it is suggested that compositions below the bold line be chosen.

AA309 in 1RNC[5]) rather than a consequence of iron content. This is probably due to the flatter thermal gradients in the Al-10 pct Si alloy that arise from the greatly extended period of eutectic solidification. The lack of a distinct transition in pore morphology in the 10 pct silicon alloy (in contrast to that previously observed in AA309) may also be rationalized on the basis of this poorer feeding response.

It is apparent that the casting conditions in the 1RNC configuration are so poor for the 10 pct silicon alloy that the iron effect is masked, unless statistically anomalous points are omitted from the analysis. Adding a second riser improves the casting performance of the alloy, which makes the test more sensitive to the iron level. Given that no anomalous points arose when the second riser was used, this suggests that it may have been preferable to employ the 2RNC configuration throughout this stage of the program, rather than the 1RNC configuration. The latter configuration had been chosen because it had clearly highlighted the iron-porosity effect in the AA309 alloy.

As for AA309, the linearly increasing sizes and number density of iron-containing intermetallic particles observed in the microstructure of the Al-10 pct Si alloy continue to suggest that it is not the presence of the β phase *per se*, but rather the point at which it forms during solidification, that is the crucial issue in determining porosity-forming behavior. The reason why this should occur is the subject of an additional article.[6]

The experimental success of using the model based on the Al-Fe-Si phase diagram as a predictive tool for the 10 pct silicon alloy suggests that it may also have wider applicability. To this end, a diagram has been constructed which plots the line of starting alloy compositions (Si and Fe) for which a Scheil-type solidification path results in the formation of the Al-Si-βAl_5FeSi ternary eutectic directly after aluminum dendrite formation, without the formation of any other intervening phase (Figure 8). For compositions below the line, the Al-Si binary eutectic will form as an intermediate phase, and iron-related shrinkage-porosity defects do not form. However, similar extended defects may form regardless of iron content if the casting conditions are sufficiently poor that they dominate porosity formation. For compositions above the line, the Al-βAl_5FeSi binary eutectic forms as the intermediate phase, and iron-related shrinkage-porosity defects are likely to form under poor casting conditions. This line allows the prediction of the critical iron content for any given silicon content through the relationship

$$Fe_{crit} \approx 0.075 \times \text{pct Si} - 0.05 \qquad [5]$$

It should be noted that both the original AA309 alloy and the present Al-10 pct Si alloy are unmodified, nongrain-refined, and contain approximately 1.2 pct Cu and 0.5 pct Mg. Caution should, therefore, be exercised in the indiscriminate extension of this predictive model to other alloy conditions.

VI. CONCLUSIONS

The onset of highly localized porosity formation during the solidification of an Al-5 pct Si alloy (AA309) only occurs at iron contents greater than 0.4 pct. For an alloy with a silicon content of 10 pct, this defect-onset composition is shifted to 0.7 pct Fe. This is explained in terms of the solidification sequence, based on segregation lines calculated using the Scheil equation. Casting is optimized when solidification proceeds directly to the ternary Al-Si-Al_5FeSi eutectic point, whereas the casting outcome is poor when solidification proceeds *via* the binary Al-Al_5FeSi eutectic valley. The critical iron content at which the porosity is minimized is a function of the silicon content of the alloy.

ACKNOWLEDGMENTS

The authors thank Comalco Aluminium Limited for permission to use the ILP casting technology in the production of the test castings. The Cooperative Research Centre for Alloy and Solidification Technology (CAST) was established under and is funded in part by the Australian Government's Cooperative Research Centre Scheme.

REFERENCES

1. M. Claude Mascré: *Fonderie*, 1955, vol. 108, pp. 4330-36.
2. H. Iwahori, H. Takamiya, K. Yonekura, Y. Yamamoto, and M. Nakamura: *Casting*, 1988, vol. 60 (9), pp. 590-95.
3. J.E. Eklund: Ph.D. Thesis, Helsinki University of Technology, Helsinki, Finland, 1993.
4. N. Roy, A.M. Samuel, and F.H. Samuel: *Metall. Mater. Trans. A*, 1996, vol. 27A, pp. 415-29.
5. J.A. Taylor, G.B. Schaffer, and D.H. StJohn: *Metall. Mater. Trans. A*, 1999, vol. 30A, pp. 1643-50.
6. J.A. Taylor, G.B. Schaffer, and D.H. StJohn: in *Metall. Mater. Trans. A*, 1999, vol. 30A, pp. 1657-62.
7. M.C. Flemings: *Solidification Processing*, McGraw-Hill Inc., New York, NY, 1974, pp. 33-36.
8. Y. Langsrud: *Proc. Int. Conf., User Aspects of Phase Diagrams*, F.H. Hayes, ed., Institute of Metals in London, 1991, Petten, The Netherlands, June 25–27, 1990, pp. 90-100.
9. L. Backerud, G. Chai, and J. Tamminen: *Solidification Characteristics of Aluminum Alloys: Vol. 2—Foundry Alloys*, AFS/Skanaluminium, Des Plaines, IL, 1990, pp. 119-26.
10. G.V. Raynor: *Phase Equilibria in Iron Ternary Alloys: A Critical Assessment of the Experimental Literature*, Institute of Metals, London, 1988, pp. 123-39.
11. H.W.L. Phillips and P.C. Varley: *J. Inst. Met.*, 1943, vol. 69, pp. 317-50.
12. M.H. Mulazimoglu, N. Tenekedjiev, B.M. Closset, and J.E. Gruzleski: *Cast Met.*, 1993, vol. 6 (1), pp. 16-28.